



**HAL**  
open science

## Self-template synthesis of ZnS/Ni<sub>3</sub>S<sub>2</sub> as advanced electrode material for hybrid supercapacitors

Yuan Zhang, Ning Cao, Min Li, Sabine Szunerits, Ahmed Addad, Pascal Roussel, Rabah Boukherroub

► **To cite this version:**

Yuan Zhang, Ning Cao, Min Li, Sabine Szunerits, Ahmed Addad, et al.. Self-template synthesis of ZnS/Ni<sub>3</sub>S<sub>2</sub> as advanced electrode material for hybrid supercapacitors. *Electrochimica Acta*, 2019, 328, pp.135065. 10.1016/j.electacta.2019.135065 . hal-03090080

**HAL Id: hal-03090080**

**<https://hal.science/hal-03090080>**

Submitted on 21 Dec 2021

**HAL** is a multi-disciplinary open access archive for the deposit and dissemination of scientific research documents, whether they are published or not. The documents may come from teaching and research institutions in France or abroad, or from public or private research centers.

L'archive ouverte pluridisciplinaire **HAL**, est destinée au dépôt et à la diffusion de documents scientifiques de niveau recherche, publiés ou non, émanant des établissements d'enseignement et de recherche français ou étrangers, des laboratoires publics ou privés.



Distributed under a Creative Commons Attribution - NonCommercial 4.0 International License

# Self-template synthesis of ZnS/Ni<sub>3</sub>S<sub>2</sub> as advanced electrode material for hybrid supercapacitors

Yuan Zhang<sup>1,#</sup>, Ning Cao<sup>2,3,#</sup>, Min Li<sup>1</sup>, Sabine Szunerits<sup>1</sup>, Ahmed Addad,<sup>4</sup> Pascal Roussel<sup>5</sup> and Rabah Boukherroub<sup>1\*</sup>

<sup>1</sup>*Univ. Lille, CNRS, Centrale Lille, ISEN, Univ. Valenciennes, UMR 8520 - IEMN, F-59000 Lille, France*

<sup>2</sup>*Key Laboratory of Unconventional oil & Gas Development, China University of Petroleum (East China), Qingdao 266580, P.R. China*

<sup>3</sup>*School of Materials Science and Engineering, China University of Petroleum (East China), Qingdao, Shandong Province, 266580, P. R. China*

<sup>4</sup>*Univ. Lille, CNRS, UMR 8207 – UMET, F-59000 Lille, France*

<sup>5</sup>*Univ. Lille, CNRS, ENSCL, Centrale Lille, Univ. Artois, UMR8181, UCCS-Unité de Catalyse et Chimie du Solide, Lille, F-59000, France*

---

# Both authors have equally contributed.

\*To whom correspondence should be send to: [rabah.boukherroub@univ-lille.fr](mailto:rabah.boukherroub@univ-lille.fr)

## Abstract

In this work, ZnS/Ni<sub>3</sub>S<sub>2</sub> electrode material was synthesized by a simple self-template approach. The synthetic route includes chemical precipitation of Zn-Ni precursor in a polyvinylpyrrolidone (PVP)/Milli-Q water solution by dropping ammonia solution and subsequent conversion of the Zn-Ni precursor to ZnS/Ni<sub>3</sub>S<sub>2</sub> via chemical reaction with thioacetamide (TAA), as the sulfur source. Here, Zn-Ni precursor can be considered as a template that is converted to ZnS/Ni<sub>3</sub>S<sub>2</sub> during the sulfidation process. The synthesized ZnS/Ni<sub>3</sub>S<sub>2</sub> material displays a porous texture and a high specific surface area. These properties are beneficial for the investigation of the developed material as electrode in supercapacitors. Indeed, the obtained ZnS/Ni<sub>3</sub>S<sub>2</sub> material exhibits improved specific capacity of 890.1 C g<sup>-1</sup> at 1 A g<sup>-1</sup> along with a good rate capability (70% retention of its initial value from 1 A g<sup>-1</sup> to 20 A g<sup>-1</sup>). Furthermore, the ZnS/Ni<sub>3</sub>S<sub>2</sub> electrode achieves a good cycling stability (~82% retention of its capacitance capacity at 10 A g<sup>-1</sup> after 6000 charging-discharging cycles). Moreover, ZnS/Ni<sub>3</sub>S<sub>2</sub> is used as a positive electrode and porous reduced graphene oxide (PrGO) as a negative electrode to assemble a hybrid supercapacitor. The fabricated hybrid supercapacitor offers a specific capacity of ~112.5 C g<sup>-1</sup> at 0.5 A g<sup>-1</sup>, and delivers an energy density of 30.6 W h kg<sup>-1</sup> at a power density of 880 W kg<sup>-1</sup>. This work not only demonstrates that ZnS/Ni<sub>3</sub>S<sub>2</sub> material can serve as an efficient electrode material for supercapacitors, but also provides an easy operation way for preparing high performance metal-sulfide electrodes for energy storage application.

**Keywords:** ZnS/Ni<sub>3</sub>S<sub>2</sub>; Self-template; Chemical precipitation; Hybrid supercapacitor.

## 1. Introduction

As convenient energy storage devices, electrochemical supercapacitors have attracted substantial attention, because they represent the most promising devices to bridge function of dielectric capacitors with high power output, and batteries/fuel cells with high energy storage [1]. Other remarkable benefits of supercapacitors are related to their ultra-long lifecycle, fast charge/discharge process and higher power density, which are all necessary for applications in digital products, hybrid electric vehicles and other portable electronic devices [2-5].

Usually, supercapacitors could be classified into either symmetric, asymmetric or hybrid supercapacitors. Generally, a symmetric supercapacitor is made up of two same electrode materials (the same material, having the same mass, thickness and so on). An asymmetric supercapacitor comprises a positive electrode and a negative electrode whenever the weight, thickness or the material is different, while a hybrid supercapacitor consists of a non-faradaic and a faradaic type electrode material such as carbonaceous and metal oxides (metal sulfides or metal hydroxides) electrode materials, respectively [6-8]. In previous reports [9, 10], hybrid supercapacitors usually provide wide operation voltage range and improved energy density. Generally, the working voltage and energy density of hybrid supercapacitors are much larger than symmetric supercapacitors. However, the practical application of hybrid supercapacitors remains limited because of the lack of suitable electrode materials with good electrochemical performance.

Recently, a huge attention has been devoted to metal sulfides electrode materials in hybrid supercapacitors, because of their appreciable stability, wide range of morphological properties and good electrical conductivity [11-13]. The usage of ZnS in energy storage devices has also been extensively investigated [14, 15]. However, like other mono-metal sulfides [13, 16, 17], ZnS experiences volume expansion and low conductivity during the cycling process, leading to

poor electrochemical performance. Bimetal sulfides are found to offer suitable performance because of enhanced electrochemical properties, better thermal and mechanical stability than that of mono-metal sulfides [5, 18, 19]. Ni-based sulfide materials have received extensive attention, because of their high theoretical specific capacitance values, rich oxidation states and cost effectiveness [20-25]. Additionally, the preparation of nickel-based bimetal sulfides/selenides has proven to enhance their electrochemical performance as electrode materials for supercapacitors. Thus, various materials such as  $\text{Ni}_3\text{S}_2@\text{Co}_9\text{S}_8$  and  $\text{NiS}@\text{NiSe}_2$  [26],  $\text{Ni}_3\text{S}_2@\beta\text{-NiS}$  [27],  $\text{Ni}_3\text{S}_2\text{-NiS}$  nanowires [28],  $\text{Ni}_3\text{S}_2\text{-Cu}_{1.8}\text{S}$  nanosheets [29], hollow  $\text{Ni}_3\text{S}_2/\text{NiS}@\text{Ni}_3\text{S}_4$  core/shell submicrospheres [30],  $\text{Ni}_3\text{S}_2\text{-NiS/N}$ -doped graphene [31] have been prepared and investigated as electrodes for supercapacitors.

Unlike nickel sulfides, the preparation of Ni-Zn electrodes has been reported only in a few reports [25, 32]. Zhao *et al.* were the first to report the synthesis of  $\text{ZnS}/\text{Ni}_3\text{S}_2@\text{Ni}$  composite with a core-shell structure using a two-step process consisting of solution reduction and template method, and applied the resulting material for electromagnetic absorption [25]. In a recent report, Li *et al.* adopted a two-step hydrothermal method to produce cactus-like  $\text{ZnS}/\text{Ni}_3\text{S}_2$  hybrid with high electrochemical performance for supercapacitors [32]. The  $\text{ZnS}/\text{Ni}_3\text{S}_2$  electrode displayed a specific capacitance of  $2093 \text{ F g}^{-1}$  at  $1 \text{ A g}^{-1}$  and a cycling stability of 64% after 5000 cycles at a current density of  $3 \text{ A g}^{-1}$ .

Compared with various synthetic routes such as hydrothermal [32, 33], solvothermal [34], electrodeposition [35], microwave-assisted approach [22] or other methods [36, 37], self-template route [38] is expected to be an effective operation method to prepare metal sulfides, because both structure and morphology of the final product are controllable and the step of template removal is avoided. Indeed, by using this technique, we were able to successfully synthesize  $\text{ZnS}/\text{Ni}_3\text{S}_2$

sulfides with a large specific capacity of  $890.1 \text{ C g}^{-1}$  at  $1 \text{ A g}^{-1}$ , good rate capability (70% retention from  $1$  to  $20 \text{ A g}^{-1}$ ), and good cycling stability ( $\sim 82\%$  of capacitance capacity retention at  $10 \text{ A g}^{-1}$ ) after 6000 charge-discharge cycles. Moreover, a hybrid supercapacitor, comprising ZnS/Ni<sub>3</sub>S<sub>2</sub> as a positive electrode and porous reduced graphene oxide as a negative electrode, achieved a specific capacity of  $\sim 112.5 \text{ C g}^{-1}$  at  $0.5 \text{ A g}^{-1}$  and an energy density of  $30.6 \text{ W h kg}^{-1}$  at a power density of  $880 \text{ W kg}^{-1}$ , making it a suitable electrode material for electrochemical energy storage devices.

## 2. Experimental

### Preparation of ZnS/Ni<sub>3</sub>S<sub>2</sub> electrode materials

ZnS/Ni<sub>3</sub>S<sub>2</sub> was prepared following the method in **Figure 1**. Briefly, a solution A was prepared by dissolution of polyvinylpyrrolidone (1 g) in Milli-Q water (15 mL) at room temperature under magnetic stirring. Separately, a solution B was prepared by successive dissolution of Zn(CH<sub>3</sub>COO)<sub>2</sub>•2H<sub>2</sub>O (1 mmol) and NiCl<sub>2</sub>•6H<sub>2</sub>O (2 mmol) in 5 mL Milli-Q water. The solutions A and B were mixed together and 286.5  $\mu\text{L}$  of ammonia (35%) were added dropwise to this mixture under vigorous magnetic stirring at room temperature. The reaction was kept overnight at  $50 \text{ }^\circ\text{C}$  in an oven. After cooling to room temperature, the formed precipitate was separated by centrifugation, rinsed copiously with ethanol and Milli-Q water until the pH of the rinsing solution is  $\sim 7$ . The resulting precipitate was re-dispersed in Milli-Q water (30 mL) for further use. An aqueous solution of thioacetamide (100 mg in 10 mL Milli-Q water) was mixed with the above solution (10 mL) at room temperature under magnetic stirring. After 30 min of stirring, the solution was heated for 5 h at  $130 \text{ }^\circ\text{C}$ . After natural cooling to room temperature, a black solid

precipitate was formed. It was separated by centrifugation, rinsed sequentially with Milli-Q water and ethanol, and dried overnight at 60 °C to give ZnS/Ni<sub>3</sub>S<sub>2</sub>.

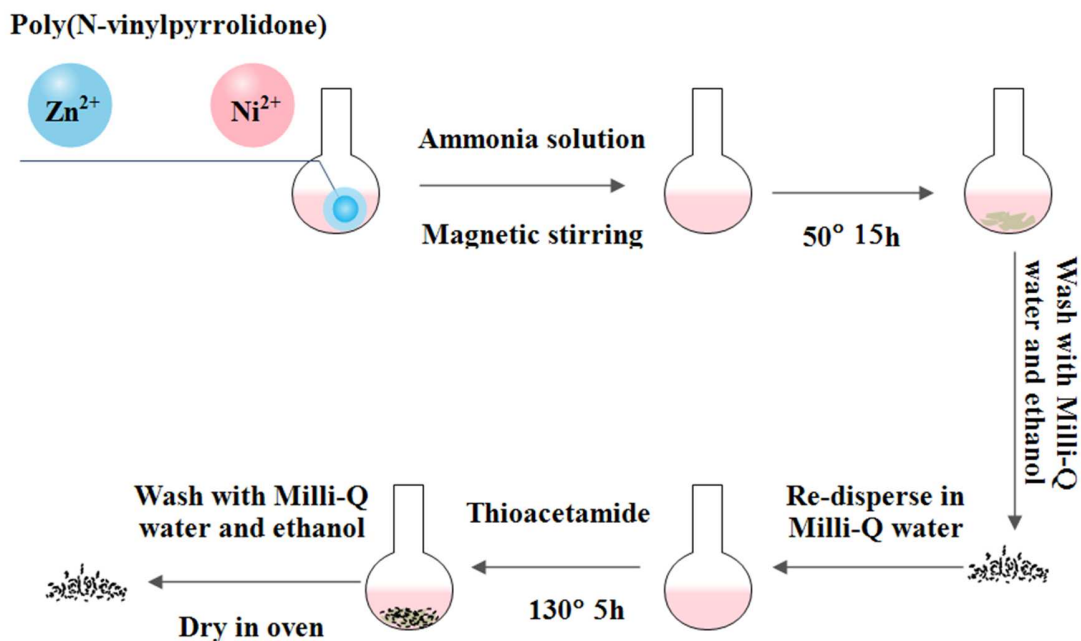


**Figure 1.** Schematic of the synthetic route of ZnS/Ni<sub>3</sub>S<sub>2</sub> electrode materials.

### 3. Results and discussion

#### 3.1 Characterization of the electrode materials

Information on the chemical composition and oxidation states of surface elements of the synthesized samples were assessed using X-ray photoelectron spectroscopy (XPS). The XPS full spectrum of the obtained ZnS/Ni<sub>3</sub>S<sub>2</sub> is depicted in **Figure 2a**, revealing the presence of Zn, Ni, and S. The presence of C, O, N in the XPS spectrum originates from residual PVP stabilizer.

The high resolution XPS spectra of the Ni, Zn and S elements are additionally provided (**Fig. 2b-d**). The Ni<sub>2p</sub> XPS high resolution spectrum of the obtained sample (**Fig. 2b**) comprises Ni<sub>2p<sub>3/2</sub></sub> and Ni<sub>2p<sub>1/2</sub></sub> spin-orbit doublets along with two shakeup satellite peaks.

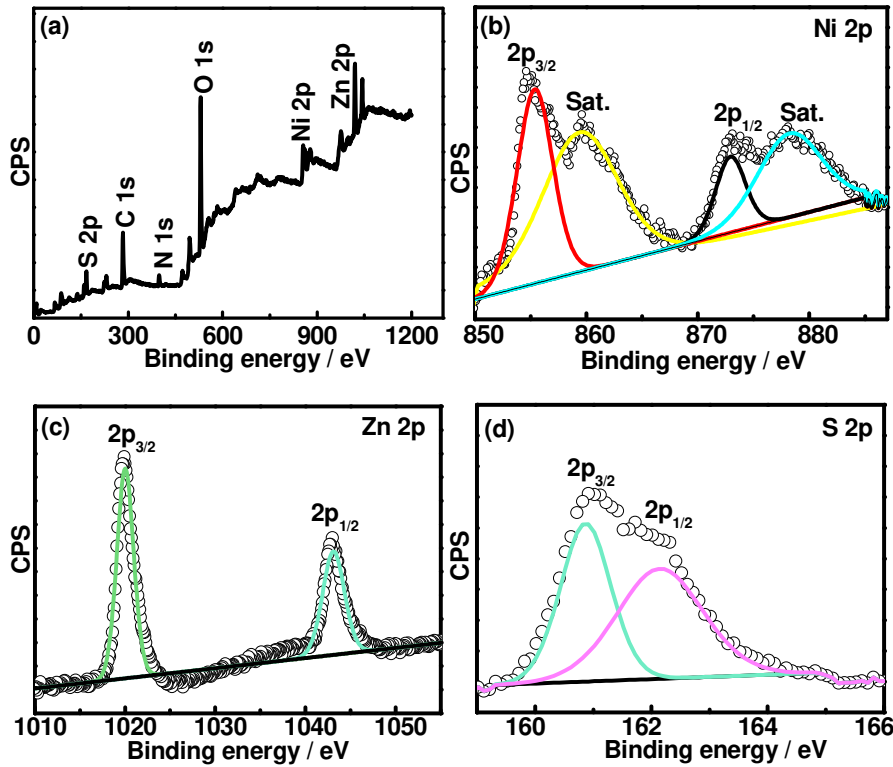


**Fig. 2.** XPS analysis of ZnS/Ni<sub>3</sub>S<sub>2</sub>: (a) full spectrum; (b), (c) and (d) are respectively the Ni<sub>2p</sub>, Zn<sub>2p</sub> and S<sub>2p</sub> high resolution spectra. “Sat” in Fig. 2b denotes satellite peaks.

The Ni<sub>2p<sub>3/2</sub></sub> at ~855.0 eV, Ni<sub>2p<sub>1/2</sub></sub> at ~872.9 eV, and the two shake-up satellite peaks at ~859.6 and ~878.5 eV are characteristic of Ni<sup>2+</sup> [39, 40]. In the Zn<sub>2p</sub> XPS high resolution spectrum (**Fig. 2c**), two strong peaks at ~1021.3 and ~1044.3 eV attributed to Zn<sup>2+</sup> are visible, suggesting the presence of Zn<sup>2+</sup> in the synthesized sample. The S<sub>2p</sub> high resolution XPS spectrum (**Fig. 2d**) can be fitted with two peaks at ~160.9 and 162.1 eV assigned to S<sub>2p<sub>3/2</sub></sub> and S<sub>2p<sub>1/2</sub></sub>, respectively [24, 41].

The crystalline phase of the as-synthesized ZnS/Ni<sub>3</sub>S<sub>2</sub> was investigated by XRD analysis (**Fig. 3a**). Two different phases could be observed. The diffraction peaks at 28.6°, 47.6° and 56.5°, attributed to the (1 1 1), (2 2 0) and (3 1 1) crystal planes, match the diffraction peaks of the face centered cubic sphalerite ZnS structure (JCPDS 05-0566) [12]. Additionally, the diffraction peaks at 2θ values of 21.8°, 31.0°, 49.4° and 55.1° are assigned to the (1 0 1), (1 1 0), (1 1 3) and (1 2 2) crystal planes of Ni<sub>3</sub>S<sub>2</sub> (JCPDS 44-1418) [39, 42, 43]. The observed diffraction peaks indicate that the product is a mixture of ZnS and Ni<sub>3</sub>S<sub>2</sub> phases.

Using the Bragg's law (Eq. 1), the interplanar distance d can be determined:

$$2d\sin\theta = n\lambda \quad (1)$$

Where d corresponds to the interplanar distance, θ represents the scattering angle, n is a positive integer, and λ=1.54056 Å.

Using equation 1, interplanar distance d values of the diffraction peaks at 2θ of 21.8°, 28.6°, 31.0°, 47.6°, 49.4°, 55.1° and 56.5° are determined to be ~0.40, 0.30, 0.28, 0.19, 0.18, 0.17 and 0.16 nm, respectively.

The crystallite size of the synthesized sample was determined using the Scherrer formula [14]:

$$D = \frac{0.94\lambda}{\beta\cos\theta} \quad (2)$$

Where β corresponds to the full width half maximum (FWHM) intensity, and λ=1.54056 Å.

Using the FWHM of the (1 1 1) peak, an average crystallite size of 8 nm was estimated.

**Figure 3b-d** depicts typical TEM images of as-prepared ZnS/Ni<sub>3</sub>S<sub>2</sub>. **Figure 3b** shows a low resolution TEM image, from which a quasi-sheet-like structure can be observed.

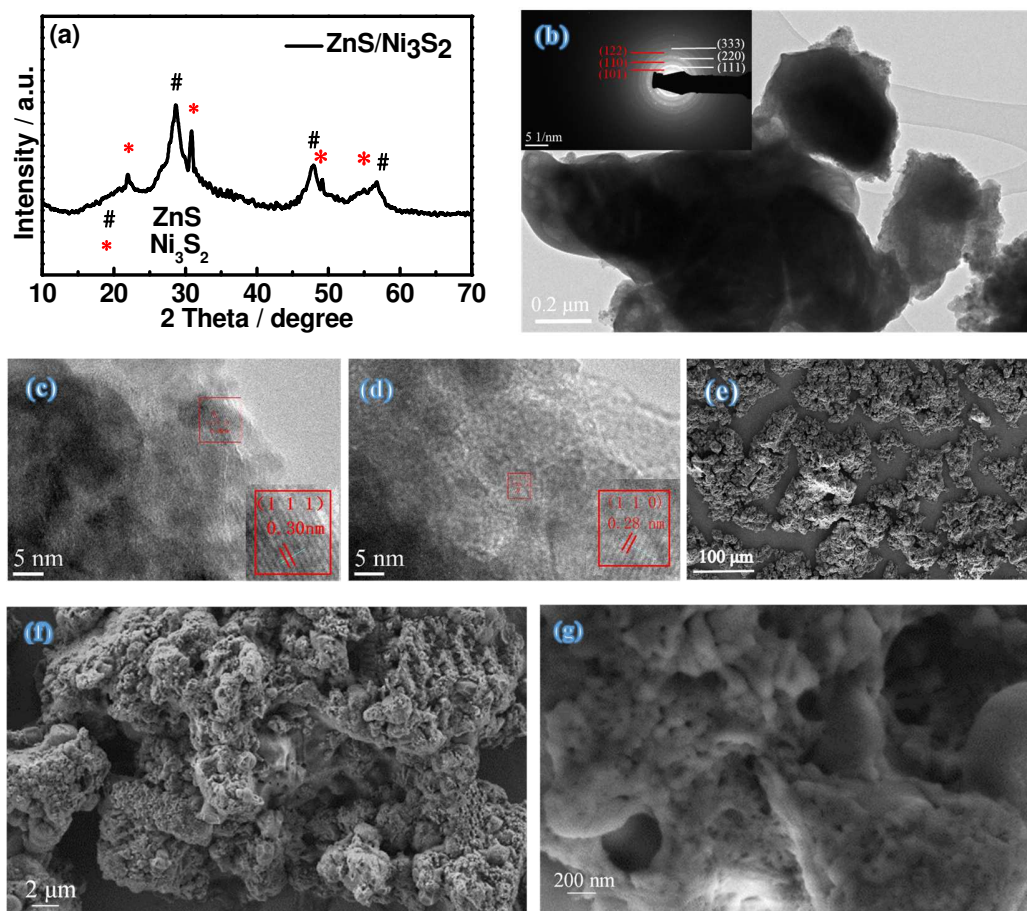


**Figure 3.** (a) XRD patterns, (b, c, d) TEM images, and (e, f, g) SEM images of ZnS/Ni<sub>3</sub>S<sub>2</sub>; the insets in (c), (d) are the HRTEM images.

Furthermore, the selected area electron diffraction (SAED) pattern reveals rings and dots, suggesting good crystallinity of the ZnS/Ni<sub>3</sub>S<sub>2</sub> nanoparticles (inset in **Fig. 3b**). The interplanar distance  $d$  values of the lattice fringes, calculated from the SAED pattern, are 0.30, 0.19, 0.16 nm, in accordance with the (1 1 1), (2 2 0), and (3 3 3) lattice planes of ZnS. Moreover, additional three lattice fringes of 0.40, 0.28, 0.17 nm due to the (1 0 1), (1 1 0) and (1 2 2) lattice planes of Ni<sub>3</sub>S<sub>2</sub> are also detected. HRTEM images of ZnS/Ni<sub>3</sub>S<sub>2</sub> are displayed in **Figure 3 c, d**. The clear lattice fringe spacing of 0.30 nm (**Fig. 3c**) matches well with the (1 1 1) lattice plane of ZnS

phase, while the lattice fringe spacing of 0.28 nm is in good accordance with the (1 1 0) lattice plane of Ni<sub>3</sub>S<sub>2</sub> phase (**Fig. 3d**). The results corroborate the XRD analysis.

SEM images of ZnS/Ni<sub>3</sub>S<sub>2</sub> are depicted in **Figure 3e-g**. Unlike the smooth surface of bare ZnS sample (**Fig. S1**), the SEM image of ZnS/Ni<sub>3</sub>S<sub>2</sub> sample, at a lower magnification, reveals that the surface is very rough, suggesting that addition of Ni enhances the surface roughness (**Fig. 3e**). Furthermore, it could be clearly observed that this rough structure is composed of numerous loose particles and porous structures (**Fig. 3f-g**). This roughness combined with a loose and porous structure is expected to provide more electroactive sites between active material and electrolyte [44, 45].

The synthesized ZnS/Ni<sub>3</sub>S<sub>2</sub> is expected to exhibit a large specific surface area (SSA), owing to its unique roughness and loose structure. Nitrogen adsorption-desorption isotherms were used to assess the SSA and porous texture of ZnS/Ni<sub>3</sub>S<sub>2</sub> (**Fig. 4**), which are identified as the typical type IV, according to the IUPAC classification. Additionally, hysteresis loops in the 0.6-0.9 relative pressure region are apparent (**Fig. 4a**). The results indicate the presence of mesoporous structures in the sample, as evidenced by the pore diameter distribution profile (**Fig. 4b**), determined from the desorption isotherm using the BJH model. The presence of a pore diameter peak at ~10 nm is a good indication of the presence of mesopores in ZnS/Ni<sub>3</sub>S<sub>2</sub>. The BET SSA of ZnS/Ni<sub>3</sub>S<sub>2</sub> is 147.9 m<sup>2</sup> g<sup>-1</sup>. The SSA of ZnS/Ni<sub>3</sub>S<sub>2</sub> sample, prepared through our method, is found to be larger than that reported for metal sulfides such as ZnS-NiS<sub>1.97</sub> (105.3 m<sup>2</sup> g<sup>-1</sup>) [18], Zn<sub>x</sub>Co<sub>1-x</sub>S (77.2 m<sup>2</sup> g<sup>-1</sup>) [36], Zn<sub>0.76</sub>Co<sub>0.24</sub>S@Ni<sub>3</sub>S<sub>2</sub> (89.1 m<sup>2</sup> g<sup>-1</sup>) [46], ZnCo<sub>2</sub>S<sub>4</sub> core-shell nanospheres (117.3 m<sup>2</sup> g<sup>-1</sup>) [47] and flowerlike Sb<sub>2</sub>S<sub>3</sub> (14.7 m<sup>2</sup> g<sup>-1</sup>) [48]. Accordingly, the porous structure and large specific surface area are necessary to achieve electrode materials with good electrochemical energy storage performance [49, 50]. Therefore, it is quite reasonable to hypothesize that the as-

synthesized ZnS/Ni<sub>3</sub>S<sub>2</sub> with such roughness and loose structure may have promising applications in electrochemical supercapacitors.

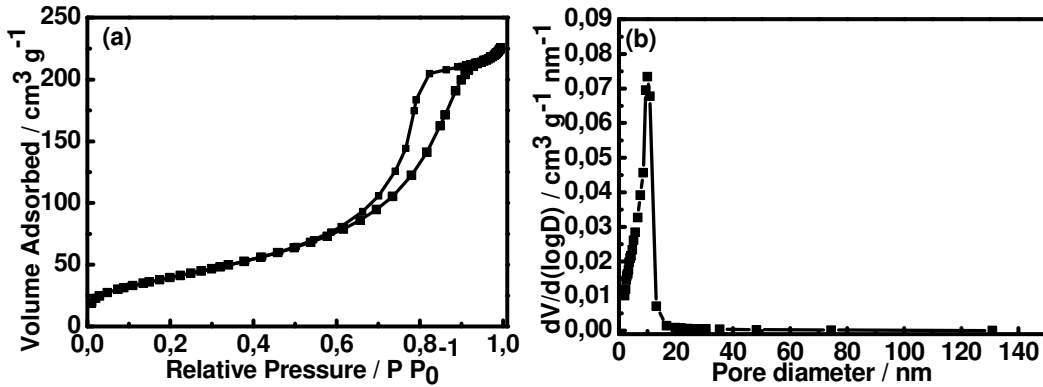


**Figure 4.** (a) Nitrogen adsorption-desorption isotherm and (b) pore size distribution curve of ZnS/Ni<sub>3</sub>S<sub>2</sub>.

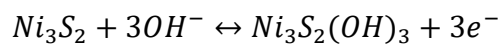
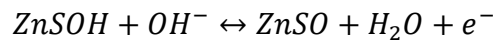
### 3.2 Electrochemical properties

In order to investigate the potential window of ZnS/Ni<sub>3</sub>S<sub>2</sub> electrode, cyclic voltammetry (CV) curves along with cathodic and anodic peak current densities *vs.* the square root of sweep rate at various scan rates (10 - 100 mV s<sup>-1</sup>) in the 0 to 0.7 V potential window are recorded (**Fig. S2**). Obviously, the CV plots exhibit obvious redox peaks (**Fig. S2a**), indicating a faradaic battery-type characteristic of the ZnS/Ni<sub>3</sub>S<sub>2</sub> electrodes [10]. Additionally, when the scan rate increases (**Fig. S2a**), the current density was enhanced without affecting the shape of the CV curves. The results suggest a good rate capability of the ZnS/Ni<sub>3</sub>S<sub>2</sub> electrode. Furthermore, when the scan rate increases, the oxidation peak shifts to high potential and the reduction peak moves towards low potential. This phenomenon is most likely due to electrochemical polarization during the surface redox reaction of the electrodes [35].

The relationship between the cathodic and anodic peak current densities *vs.* the square root of sweep rate (**Fig. S2b**) is also recorded to determine if the capacity is related to surface redox processes or bulk diffusion. The linear relationship confirms that the redox reactions of ZnS/Ni<sub>3</sub>S<sub>2</sub> were under OH<sup>-</sup> diffusion control rather than surface redox processes [51].

CV curves of ZnS/Ni<sub>3</sub>S<sub>2</sub> electrodes over different potential windows are also recorded at a scan rate of 50 mV s<sup>-1</sup> (**Fig. S2c**). Redox peaks, observed in all CV curves, are attributed to the electrochemical redox reactions of M (Zn, Ni) species at the interfaces between electrolyte and electrode. However, when the potential window is extended above +0.6 V, a significant increase of the current attributed to oxygen evolution reaction (OER) is observed. A potential window (0 to +0.55 V) and a scan rate ranging from 5 to 50 mV s<sup>-1</sup> were chosen to avoid the polarization and OER of the prepared ZnS/Ni<sub>3</sub>S<sub>2</sub> electrode.

Furthermore, the CV curves of ZnS/Ni<sub>3</sub>S<sub>2</sub> electrode and bare nickel foam are measured at the scan rate of 10 mV s<sup>-1</sup> in the potential range of 0 to +0.55 V (**Fig. S3**). The CV curve of bare nickel foam is almost a straight line, indicating that the capacity of bare nickel foam is almost negligible under our experimental conditions. The redox peaks observed in the CV curve of ZnS/Ni<sub>3</sub>S<sub>2</sub> electrode, are likely due to the reversible faradaic redox reaction of M (Zn, Ni)S-OH. Therefore, redox peaks seen in the CV curve of ZnS/Ni<sub>3</sub>S<sub>2</sub> electrode are attributed to the following faradaic redox reactions [14, 46, 52, 53]:



Faradaic battery-type behavior of the ZnS/Ni<sub>3</sub>S<sub>2</sub> electrode was investigated by recording CV plots at different scan rates (5 - 50 mV s<sup>-1</sup>) (**Fig. 5a**). Redox peaks could also be seen in the CV curves in the potential window of 0 - +0.55 V, indicating faradaic battery-type behavior of the electrode. The position of anodic and cathodic peaks for ZnS/Ni<sub>3</sub>S<sub>2</sub> electrode are given in **Table S1**.

**Figure 5b** depicts the GCD plots of ZnS/Ni<sub>3</sub>S<sub>2</sub> electrode within the current density span of 1 to 20 A g<sup>-1</sup>. Clear potential plateaus, due to the electrochemical redox reactions of M (Zn, Ni) species at the interfaces between electrolyte and electrode, are visible in the charge and discharge processes of all GCD curves. The potential plateaus in GCD curves match the redox characteristics observed in the CV curves, indicating strong faradaic battery-type characteristics of the electrode. All GCD plots provide almost symmetric characteristics, revealing the good charge-discharge coulombic efficiency during electrochemical capacitive and reversible redox processes of the prepared ZnS/Ni<sub>3</sub>S<sub>2</sub> electrode.

The specific capacity (~~specific capacitance~~) values, determined from the GCD curves (**Fig. 5b**), are displayed in **Figure 5c**. The ZnS/Ni<sub>3</sub>S<sub>2</sub> electrode provides specific capacity (~~specific capacitance~~) values of 890.1, 742.0, 726.5, 700.8, 677.8, 653.1, 632.2, and 620.1 C g<sup>-1</sup> corresponding to ~~1618.4, 1349, 1320.9, 1274.2, 1232.3, 1187.4, 1149.4, and 1127.5 F g<sup>-1</sup>~~ at current densities of 1, 2, 3, 5, 7, 10, 15, 20 A g<sup>-1</sup>, respectively. When the current density increases from 1 to 20 A g<sup>-1</sup>, the ZnS/Ni<sub>3</sub>S<sub>2</sub> electrode retained about 70% of its initial specific ~~capacitance~~ capacity value, revealing a good rate capability. Moreover, the specific capacity (~~capacitance~~) of ZnS/Ni<sub>3</sub>S<sub>2</sub> electrode is superior to that of many metal sulfide-based electrode materials and slightly lower to that reported for cactus-like ZnS/Ni<sub>3</sub>S<sub>2</sub> prepared by a two-step hydrothermal

method (**Table 1**). Such a desirable performance of the ZnS/Ni<sub>3</sub>S<sub>2</sub> electrode indicates its potential usage for energy storage devices.

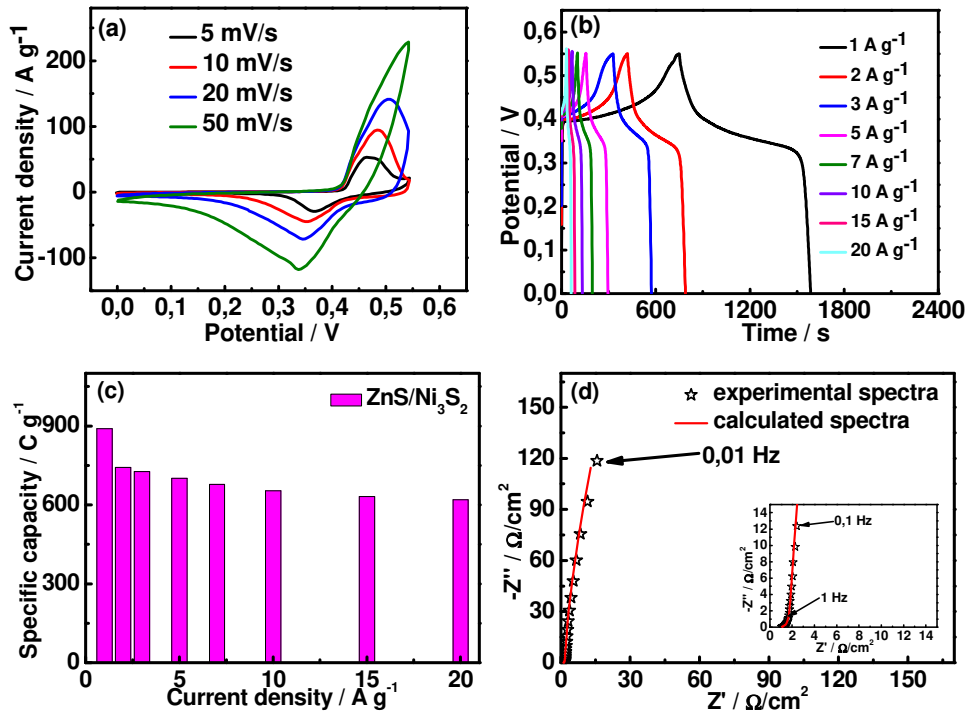


**Figure 5.** Electrochemical properties of ZnS/Ni<sub>3</sub>S<sub>2</sub> electrode in 2 M KOH: (a) CV curves at different scan rates (5 to 50 mV s<sup>-1</sup>), potential=0 - 0.55V; (b) GCD profiles at a current density of 1, 2, 3, 5, 7, 10, 15 and 20 A g<sup>-1</sup>; (c) the corresponding specific capacities within the current density span of 1 to 20 A g<sup>-1</sup>; (d) Nyquist plots.

It is well known that electrochemical impedance spectroscopy (EIS) is an extremely informative method for electrochemical nature (the charge transfer and the capacity) of electrode materials used in electrochemical supercapacitors. Therefore, EIS analysis was used to investigate the frequency-dependent behavior of ZnS/Ni<sub>3</sub>S<sub>2</sub> electrode materials. **Figure 5d** depicts the Nyquist plots with frequencies of some selected points and the corresponding fitted spectra of ZnS/Ni<sub>3</sub>S<sub>2</sub> electrode. An equivalent circuit, based on reported works [54-57], and the

corresponding calculated circuit parameters are also depicted in **Figure S4** and **Table S2**, respectively. In the fitted equivalent circuit,  $R_s$  denotes the series resistance, including the resistance of inherent active material, electrolyte resistance and the contact resistance.  $R_{ct}$ , and CPE are assigned to the faradaic charge transfer resistance and constant phase element accounting for the faradaic pseudocapacitor capacitance capacity.  $C_F$  and  $W$  represent the faradaic capacitance and Warburg resistance (diffusion resistance), respectively. According to the fitted equivalent circuit, the obtained series resistance ( $R_s$ ), related to the high frequency region  $>10^4$  Hz (intercept at the real axis), is about  $1.03 \Omega/\text{cm}^2$ ; the charge transfer resistance ( $R_{ct}$ ), related to the depressed-semicircle in the high-to-medium frequency region ( $10^4$  to 1 Hz), is about  $1.01 \Omega/\text{cm}^2$ . The appearance of CPE may be attributed to the porosity of the prepared ZnS/Ni<sub>3</sub>S<sub>2</sub> electrode material and the calculated value is about  $0.26 \text{ sec}^{1/n}/\text{cm}^2$  ( $n=0.47$ ) and the faradaic capacitance is found to be  $0.13 \text{ F}/\text{cm}^2$ . Moreover, in the lower frequency region ( $< 1$  Hz), the inclined line of the Warburg line, which is related to the electrolyte ion ( $\text{OH}^-$ ) diffusion from the electrolyte (2 M KOH) into the loose and porous ZnS/Ni<sub>3</sub>S<sub>2</sub> electrode surface [58], represents a low diffusion resistance of  $0.0046 \text{ sec}^{1/2}/\text{cm}^2$ . The slope of the Warburg line is higher than  $45^\circ$ , indicating the easy access of  $\text{OH}^-$  electrolyte for fast and reversible faradaic redox reaction and more ideal capacitor behavior [59, 60], which further confirms that the ZnS/Ni<sub>3</sub>S<sub>2</sub> electrode can retain good capacitive performance.

**Table 1.** Comparison of the specific capacity values of metal-sulfide-based electrode materials for energy storage applications.

Electrode material	Specific capacitance (F g <sup>-1</sup> )	Specific capacity (C g <sup>-1</sup> )	Capacity retention (%)	Ref
Zn <sub>0.76</sub> Co <sub>0.24</sub> S	486.2 ( <del>2.0 A g<sup>-1</sup></del> )	-	86.4 (2k cycles at 5.0 A g <sup>-1</sup> )	[36]
rGO-Ni <sub>3</sub> S <sub>2</sub>	-	616.0 (1.0 A g <sup>-1</sup> )	92.7 (5k cycles at 5.0 A g <sup>-1</sup> )	[61]
Ni <sub>3</sub> S <sub>2</sub> /carbon nanotube	800.0 ( <del>3.2 A g<sup>-1</sup></del> )	-	80 (1k cycles at 3.2 A g <sup>-1</sup> )	[62]
ZnCo <sub>2</sub> S <sub>4</sub>	1045.3 ( <del>2.0 A g<sup>-1</sup></del> )	-	95.5 (5k cycles at 4.0 A g <sup>-1</sup> )	[47]
ZnS-NiS <sub>2</sub>	970.0 ( <del>2.0 A g<sup>-1</sup></del> )	-	87 (1k cycles at 5.0 A g <sup>-1</sup> )	[63]
NiS <sub>2</sub>	1725.0 ( <del>5 A g<sup>-1</sup></del> )	-	123.0% (10k cycles at 20.0 A g <sup>-1</sup> )	[64]
Zn <sub>x</sub> Ni <sub>1-x</sub> S/NF	1412.0 ( <del>1.0 A g<sup>-1</sup></del> )	-	81.5 (4k cycles at 2.0 A g <sup>-1</sup> )	[65]
ZnS-NiS <sub>1.97</sub>	-	696.8 (5.0 A g <sup>-1</sup> )	Less 5.5% loss (6k cycles at 10.0 A g <sup>-1</sup> )	[18]
Co-S-80	285.0 ( <del>0.5 A g<sup>-1</sup></del> )	-	86.5 (1k cycles at 0.5 A g <sup>-1</sup> )	[11]
ZnS/Ni <sub>3</sub> S <sub>2</sub>	2093 ( <del>1.0 A g<sup>-1</sup></del> )	-	64 (5k cycles at 3.0 A g <sup>-1</sup> )	[32]
<b>ZnS/Ni<sub>3</sub>S<sub>2</sub></b>	<b>1618.4</b> <b>(<del>1.0 A g<sup>-1</sup></del>)</b>	<b>890.1</b> <b>(1.0 A g<sup>-1</sup>)</b>	<b>81.7</b> <b>(6k cycles at 10.0 A g<sup>-1</sup>)</b>	<b>Our work</b>

The cycling stability of ZnS/Ni<sub>3</sub>S<sub>2</sub> electrode was established by repeated 6000 charge/discharge cycles at a current density of 10 A g<sup>-1</sup> (**Fig. 6a**). Encouragingly, the retention of the ZnS/Ni<sub>3</sub>S<sub>2</sub> electrode is about 82% of its initial capacitance capacity after 6000 charge/discharge cycles, which is better than 64% achieved by cactus-like ZnS/Ni<sub>3</sub>S<sub>2</sub> at 3 A g<sup>-1</sup> [32].

XPS analysis was conducted to assess the chemical changes that have occurred during the stability test. **Figure 6b** depicts the XPS high resolution spectrum of the Ni<sub>2p</sub> of the ZnS/Ni<sub>3</sub>S<sub>2</sub> electrode after 6000 charge-discharge cycles. The spectrum can be deconvoluted with two spin-orbit peaks at 856.4 and 874.3 eV assigned to Ni<sup>2+</sup><sub>2p3/2</sub> and Ni<sup>2+</sup><sub>2p1/2</sub>, respectively. The presence of two satellite peaks (~862.1 and 880.1 eV), characteristic of Ni<sup>2+</sup>, reveals the excellent reversible redox process during charge-discharge cycling.

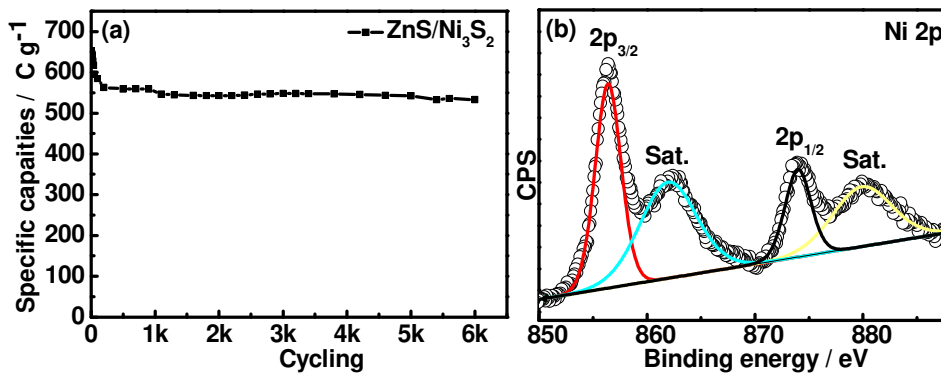


**Figure 6.** (a) Stability test of ZnS/Ni<sub>3</sub>S<sub>2</sub> electrode at 10 A g<sup>-1</sup> for 6000 cycles; (b) Ni<sub>2p</sub> high resolution XPS spectrum after 6000 cycles. “Sat” in Figure 6b denotes satellite peaks.

### 3.3 Fabrication of a hybrid supercapacitor

Hybrid supercapacitors are believed to combine the advantage of faradaic battery-type electrode material as a positive electrode and double-layer capacitor electrode material as a negative electrode; the combination of these two types of electrode materials is supposed to be able to enlarge the cell's operating voltage greatly and thus improve its energy density [9, 10, 66]. To further assess the practical utilization of the prepared ZnS/Ni<sub>3</sub>S<sub>2</sub> electrode, a hybrid supercapacitor was assembled using ZnS/Ni<sub>3</sub>S<sub>2</sub> electrode material as a positive electrode and porous reduced graphene oxide (PrGO) electrode material as a negative electrode. The prepared PrGO electrode material has interesting features such as a porous structure (see TEM image in **Fig. S5**), mandatory to achieve efficient negative electrode materials. The electrochemical performance of PrGO electrode material is also depicted in **Figure S6**. The absence of redox peaks in the CV curves along with the triangle shape of the charge and discharge curves reveal that the PrGO electrode store energy through double-layer capacitance.

A 3-electrode system was used to determine the optimal operating potential window of the hybrid supercapacitor based on the ZnS/Ni<sub>3</sub>S<sub>2</sub> and PrGO working potential range. **Figure 7a** depicts the working potential window vs. Hg/HgO of ZnS/Ni<sub>3</sub>S<sub>2</sub> (0 to +0.55 V) and PrGO (-0.9 to +0.1 V) at a scan rate of 10 mV s<sup>-1</sup>. Based on these values, the cell voltage of the fabricated hybrid supercapacitor was fixed at 1.5 V.

**Figure 7b** displays a series of CV curves of the hybrid supercapacitor at different cell voltages at a scan rate=50 mV s<sup>-1</sup>. Interestingly, increasing the cell voltage does not seem to affect the shape of the CV curves. Additionally, redox peaks are obvious for all investigated potential windows. However, the polarization becomes much more obvious as the cell voltage was extended to 1.8 V. GCD curves were also recorded at various cell voltage values (current density=5 A g<sup>-1</sup>) to determine the power density (P) an energy density (E) (**Fig. S7**). It could be

clearly seen that higher the applied cell voltage, larger energy density the hybrid supercapacitor could offer ( $30.9 \text{ W h kg}^{-1}$  at 1.8 V,  $26.7 \text{ W h kg}^{-1}$  at 1.6 V and  $18.2 \text{ W h kg}^{-1}$  at 1.5 V). Both CV and GCD analysis indicated that the PrGO//ZnS/Ni<sub>3</sub>S<sub>2</sub> hybrid supercapacitor operating potential window could be extended up to 1.8 V. However, a cell voltage of 1.6 V was used for further investigation of the electrochemical properties of the PrGO//ZnS/Ni<sub>3</sub>S<sub>2</sub> hybrid supercapacitor, considering the energy density and the polarization of assembled hybrid supercapacitor.

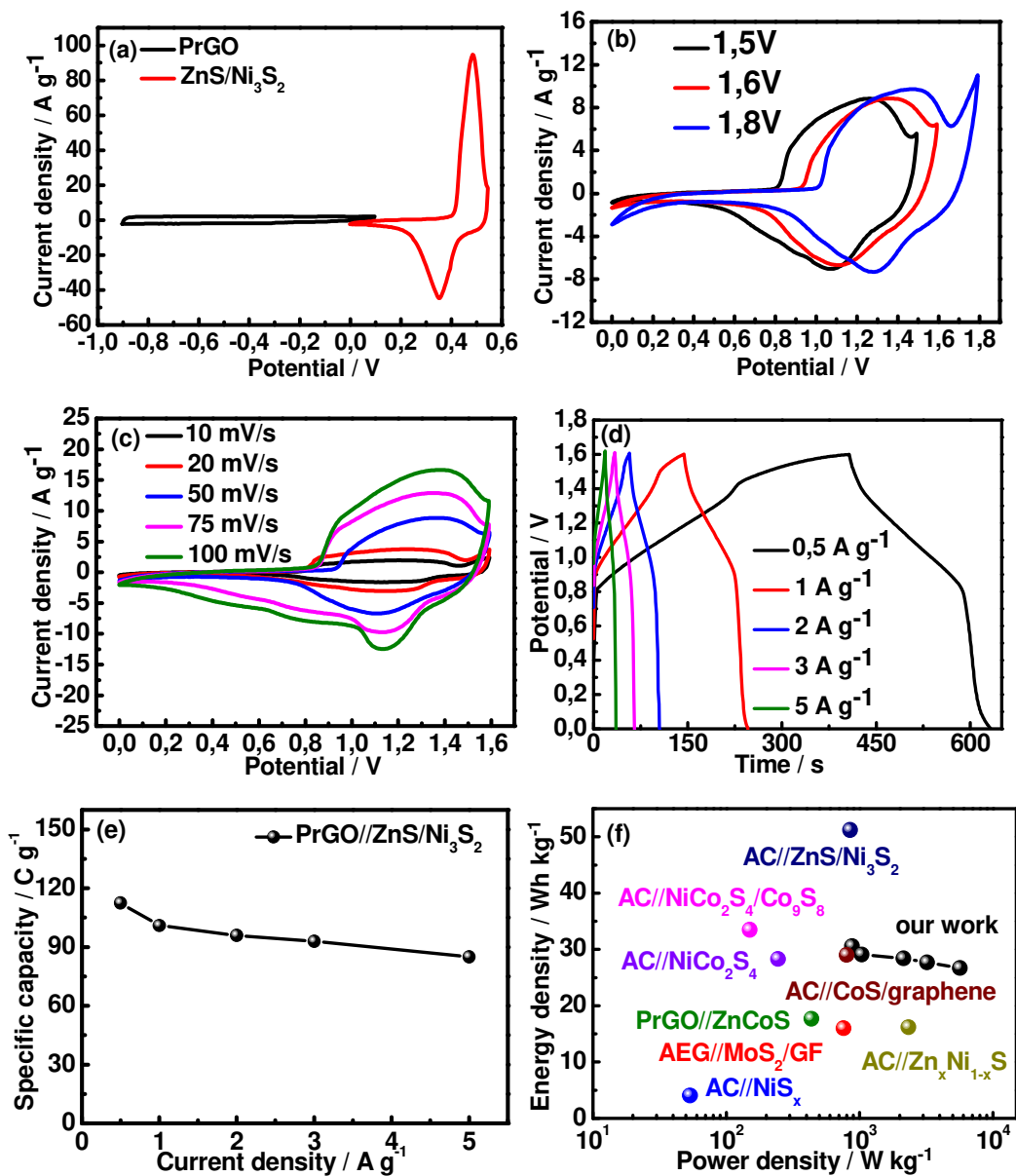


**Figure 7.** (a) CV curves of the positive and negative electrodes at a scan rate of 10 mV s<sup>-1</sup>; (b) CV curves recorded at different cell voltages; (c) CV curves at different scan rates; (d) GCD curves recorded as a function of current density; (e) the corresponding specific capacity as a function of current density; (f) typical Ragone plot of the hybrid supercapacitor.

The CV curves of the PrGO//ZnS/Ni<sub>3</sub>S<sub>2</sub> hybrid supercapacitor vs. the scan rate (10 to 100 mV s<sup>-1</sup>) at a cell voltage of 1.6 V are displayed in **Figure 7c**. Again, under these experimental conditions, the shape of the CV curves is not altered. The GCD curves (**Fig. 7d**) of the hybrid supercapacitor were also recorded to estimate the specific capacity, power density (P) and energy density (E). The change of the specific capacity, determined from the GCD curves, is summarized in **Figure 7e**. The hybrid supercapacitor exhibited a maximum specific capacitance capacity of 112.5 C g<sup>-1</sup> at a current density of 0.5 A g<sup>-1</sup>. Additionally, in **Figure 7f** is depicted the Ragone plot of the PrGO//ZnS/Ni<sub>3</sub>S<sub>2</sub> hybrid supercapacitor. The hybrid supercapacitor exhibited relatively high energy density and power density values of ~30.6 W h kg<sup>-1</sup> and ~880 W kg<sup>-1</sup> at 0.5 A g<sup>-1</sup>, respectively. The performance of the hybrid supercapacitor was also good even at a high current density of 5 A g<sup>-1</sup>; indeed, the hybrid supercapacitor attained an energy density of ~26.7 W h kg<sup>-1</sup> at a high power density of ~5659 W h kg<sup>-1</sup>. These values are comparable to and even better than those reported in the literature for many other supercapacitor devices and slightly lower than 51.2 Wh kg<sup>-1</sup> at 849.4 W kg<sup>-1</sup> recorded using cactus-like ZnS/Ni<sub>3</sub>S<sub>2</sub> (**Table 2**).

**Table 2.** Comparison with other metal sulfide hybrid supercapacitors.

Electrode material	Working voltage / V	Energy density / Wh kg <sup>-1</sup>	Power density / W kg <sup>-1</sup>	Reference
Active carbon (AC)//CoS/graphene	1.6	29	800	[67]
AC//NiS <sub>x</sub>	1.6	4.1	53.5	[44]

PrGO//ZnCoS	1.5	17.7	435	[68]
AC//NiCo <sub>2</sub> S <sub>4</sub>	1.5	28.3	245	[59]
AEG//MoS <sub>2</sub> /GF	1.4	16	758	[7]
AC//Zn <sub>x</sub> Ni <sub>1-x</sub> S	1.6	16.2	2330	[21]
AC//NiCo <sub>2</sub> S <sub>4</sub> /Co <sub>9</sub> S <sub>8</sub>	1.5	33.5	150	[41]
AC//ZnS/Ni <sub>3</sub> S <sub>2</sub>	1.6	51.2	849.4	[32]
<b>PrGO//ZnS/Ni<sub>3</sub>S<sub>2</sub></b>	<b>1.6</b>	<b>30.6</b>	<b>880</b>	<b>Our work</b>

The practical application of the asymmetric supercapacitor is further demonstrated through powering yellow, red and green LEDs using two asymmetric supercapacitors connected in series. As can be seen in **Figure 8**, the yellow, red and green LEDs can be sequentially illuminated upon connection to fully charged supercapacitors.



**Figure 8:** Photographs of LEDs (yellow, red and green) powered by two asymmetric supercapacitors connected in series.

#### 4. Conclusion

In summary, ZnS/Ni<sub>3</sub>S<sub>2</sub> electrode material with high specific surface area was synthesized using a self-template method. The ZnS/Ni<sub>3</sub>S<sub>2</sub> electrode exhibited a high specific capacity of 890.1 C g<sup>-1</sup> at 1 A g<sup>-1</sup>, with good cycling stability (~82% of capacitance capacity retention) at a current density of 10 A g<sup>-1</sup> after 6000 cycles in 2M KOH aqueous electrolyte. Furthermore, a

PrGO//ZnS/Ni<sub>3</sub>S<sub>2</sub> hybrid supercapacitor was fabricated to investigate the potential usage of the developed material for energy storage. Under optimized cell voltage window (1.6 V), the hybrid supercapacitor achieved a good electrochemical performance such as a good energy density of 30.6 W h kg<sup>-1</sup> at a power density of 880 W kg<sup>-1</sup>. Moreover, for practical application, yellow, red and green LED could be powered sequentially by using two ASC connected in series. The results reported in the present work hold promise for practical application of ZnS/Ni<sub>3</sub>S<sub>2</sub> as an anode material for assembling high performance hybrid supercapacitors.

### **Acknowledgements**

Financial support is acknowledged from the Centre National de la Recherche Scientifique (CNRS), the University of Lille, and the Hauts-de-France region. N.C. thanks the National Natural Science Foundation of China (grants No.51701240), Key Research and Development Program of Shandong Province (grant No.2017GGX20123) and the Fundamental Research Funds for the Central Universities (grant No.19CX05001A) for financial support. Y.Z. thanks the Chinese government for the China Scholarship Council Award.

### **References**

[1] G. Wang, L. Zhang, J. Zhang, A review of electrode materials for electrochemical supercapacitors, *Chem. Soc. Rev.* 41 (2012) 797-828.

- [2] S. Min, C. Zhao, G. Chen, Z. Zhang, X. Qian, One-pot Hydrothermal Synthesis of 3D Flower-like RGO/Co<sub>3</sub>O<sub>4</sub>/Ni(OH)<sub>2</sub> Composite Film on Nickel Foam for High-performance Supercapacitors, *Electrochim. Acta* 135 (2014) 336-344.
- [3] L. Liu, Z. Niu, J. Chen, Unconventional supercapacitors from nanocarbon-based electrode materials to device configurations, *Chem. Soc. Rev.* 45 (2016) 4340-4363.
- [4] C. Liu, F. Li, L. P. Ma, H. M. Cheng, Advanced materials for energy storage, *Adv. Mater.* 22 (2010) E28-E62.
- [5] Y. Zhu, X. Chen, W. Zhou, K. Xiang, W. Hu, H. Chen, Controllable preparation of highly uniform CuCo<sub>2</sub>S<sub>4</sub> materials as battery electrode for energy storage with enhanced electrochemical performances, *Electrochim. Acta* 249 (2017) 64-71.
- [6] Y. Zhang, H. Feng, X. Wu, L. Wang, A. Zhang, T. Xia, H. Dong, X. Li, L. Zhang, Progress of electrochemical capacitor electrode materials: A review, *Int. J. Hydrogen Energ.* 34 (2009) 4889-4899.
- [7] T. Masikhwa, M. Madito, A. Bello, J. Dangbegnon, N. Manyala, High performance asymmetric supercapacitor based on molybdenum disulphide/graphene foam and activated carbon from expanded graphite, *J. Colloid Interf. Sci.* 488 (2017) 155-165.
- [8] A. Jagadale, V. Kumbhar, D. Dhawale, C. Lokhande, Performance evaluation of symmetric supercapacitor based on cobalt hydroxide [Co(OH)<sub>2</sub>] thin film electrodes, *Electrochim. Acta* 98 (2013) 32-38.
- [9] W. Jin, G. Cao, J. Sun, Hybrid supercapacitor based on MnO<sub>2</sub> and columned FeOOH using Li<sub>2</sub>SO<sub>4</sub> electrolyte solution, *J. Power Sources* 175 (2008) 686-691.

- [10] M. Lukatskaya, B. Dunn, Y. Gogotsi, Multidimensional materials and device architectures for future hybrid energy storage, *Nat. Commun.* 7 (2016) 12647.
- [11] H. Wan, X. Ji, J. Jiang, J. Yu, L. Miao, L. Zhang, S. Bie, H. Chen, Y. Ruan, Hydrothermal synthesis of cobalt sulfide nanotubes: The size control and its application in supercapacitors, *J. Power Sources* 243 (2013) 396-402.
- [12] M. Javed, J. Chen, L. Chen, Y. Xi, C. Zhang, B. Wan, C. Hu, Flexible full-solid state supercapacitors based on zinc sulfide spheres growing on carbon textile with superior charge storage, *J. Mater. Chem. A* 4 (2016) 667-674.
- [13] A. Wang, H. Wang, S. Zhang, C. Mao, J. Song, H. Niu, B. Jin, Y. Tian, Controlled synthesis of nickel sulfide/graphene oxide nanocomposite for high-performance supercapacitor, *Appl. Surf. Sci.* 282 (2013) 704-708.
- [14] R. Ramachandran, M. Saranya, P. Kollu, B. Raghupathy, S. Jeong, A. Grace, Solvothermal synthesis of Zinc sulfide decorated Graphene (ZnS/G) nanocomposites for novel Supercapacitor electrodes, *Electrochim. Acta* 178 (2015) 647-657.
- [15] H. Yan, T. Li, Y. Lu, J. Cheng, T. Peng, J. Xu, L. Yang, X. Hua, Y. Liu, Y. Luo, Template-free synthesis of ordered ZnO@ZnS core-shell arrays for high performance supercapacitors, *Dalton Trans.* 45 (2016) 17980-17986.
- [16] D. Jiang, Q. Xu, S. Meng, C. Xia, M. Chen, Construction of cobalt sulfide/graphitic carbon nitride hybrid nanosheet composites for high performance supercapacitor electrodes, *J. Alloy. Compd.* 706 (2017) 41-47.

- [17] B. Chen, R. Li, G. Ma, X. Gou, Y. Zhu, Y. Xia, Cobalt sulfide/N,S codoped porous carbon core-shell nanocomposites as superior bifunctional electrocatalysts for oxygen reduction and evolution reactions, *Nanoscale* 7 (2015) 20674-20684.
- [18] C. Wei, Q. Ru, X. Kang, H. Hou, C. Cheng, D. Zhang, Self-template synthesis of double shelled ZnS-NiS<sub>1.97</sub> hollow spheres for electrochemical energy storage, *Appl. Surf. Sci.* 435 (2018) 993-1001.
- [19] Y. Sui, Y. Zhang, H. Hu, Q. Xu, F. Yang, Z. Li, High Energy Density Asymmetric Supercapacitor Based ZnS/NiCo<sub>2</sub>S<sub>4</sub>/Co<sub>9</sub>S<sub>8</sub> Nanotube Composites Materials, *Adv. Mater. Interfaces* 5 (2018) 1800018.
- [20] Y. Liu, J. Zhang, S. Wang, K. Wang, Z. Chen, Q. Xu, Facilely constructing 3D porous NiCo<sub>2</sub>S<sub>4</sub> nanonetworks for high-performance supercapacitors, *New J. Chem.* 38 (2014) 4045-4048.
- [21] X. Miao, W. Wang, Z. Wang, Hydrothermal Synthesis of Zn<sub>x</sub>Ni<sub>1-x</sub>S nanosheets for hybrid supercapacitor applications, *ChemPlusChem* 82 (2017) 1145-1152.
- [22] S. Nandhini, A. Mary, G. Muralidharan, Facile microwave-hydrothermal synthesis of NiS nanostructures for supercapacitor applications, *Appl. Surf. Sci.* 449 (2018) 485-491.
- [23] L. Yu, B. Yang, Q. Liu, J. Liu, X. Wang, D. Song, J. Wang, X. Jing, Interconnected NiS nanosheets supported by nickel foam: Soaking fabrication and supercapacitors application, *J. Electroanal. Chem.* 739 (2015) 156-163.
- [24] X. Chen, D. Chen, X. Guo, R. Wang, H. Zhang, Facile Growth of Caterpillar-like NiCo<sub>2</sub>S<sub>4</sub> Nanocrystal Arrays on Nickel Foam for High-Performance Supercapacitors, *ACS Appl. Mater. Inter.* 9 (2017) 18774-18781.

- [25] B. Zhao, G. Shao, B. Fan, W. Zhao, S. Zhang, K. Guan, R. Zhang, In situ synthesis of novel urchin-like ZnS/Ni<sub>3</sub>S<sub>2</sub>@Ni composite with a core-shell structure for efficient electromagnetic absorption, *J. Mater. Chem. C* 3 (2015) 10862-10869.
- [26] W. Wei, L. Mi, Y. Gao, Z. Zheng, W. Chen, X. Guan, Partial Ion-Exchange of Nickel-Sulfide-Derived Electrodes for High Performance Supercapacitors, *Chem. Mater.* 26 (2014) 3418-3426.
- [27] W. Li, S. Wang, L. Xin, M. Wu, X. Lou, Single-crystal  $\beta$ -NiS nanorod arrays with a hollow-structured Ni<sub>3</sub>S<sub>2</sub> framework for supercapacitor applications, *J. Mater. Chem. A* 4 (2016) 7700-7709.
- [28] X. Zang, Z. Dai, J. Yang, Y. Zhang, W. Huang, X. Dong, Template-Assisted Synthesis of Nickel Sulfide Nanowires: Tuning the Compositions for Supercapacitors with Improved Electrochemical Stability, *ACS Appl. Mater. Inter.* 8 (2016) 24645-24651.
- [29] Y. Liu, G. Liu, X. Nie, A. Pan, S. Liang, T. Zhu, In situ formation of Ni<sub>3</sub>S<sub>2</sub>-Cu<sub>1.8</sub>S nanosheets to promote hybrid supercapacitor performance, *J. Mater. Chem. A* 7 (2019) 11044-11052.
- [30] L. Cheng, Y. Hu, L. Ling, D. Qiao, S. Cui, Z. Jiao, One-step controlled synthesis of hierarchical hollow Ni<sub>3</sub>S<sub>2</sub>/NiS@Ni<sub>3</sub>S<sub>4</sub> core/shell submicrospheres for high-performance supercapacitors, *Electrochim. Acta* 283 (2018) 664-675.
- [31] Y. Luo, W. Que, C. Yang, Y. Tian, Y. Yang, X. Yin, Nitrogen-doped graphene/multiphase nickel sulfides obtained by Ni-C<sub>3</sub>N<sub>3</sub>S<sub>3</sub> (metallopolymer) assisted synthesis for high-performance hybrid supercapacitors, *Electrochim. Acta* 301 (2019) 332-341.

- [32] X. Li, J. Sun, L. Feng, L. Zhao, L. Ye, W. Zhang, D. L., Cactus-like ZnS/Ni<sub>3</sub>S<sub>2</sub> hybrid with high electrochemical performance for supercapacitors, *J. Alloy. Compd.* 753 (2018) 508-516.
- [33] H. Tong, W. Bai, S. Yue, Z. Gao, L. Lu, L. Shen, S. Dong, J. Zhu, J. He, X. Zhang, Zinc cobalt sulfide nanosheets grown on nitrogen-doped graphene/carbon nanotube film as a high-performance electrode for supercapacitors, *J. Mater. Chem. A* 4 (2016) 11256-11263.
- [34] N. Parveen, S. Ansari, S. Ansari, H. Fouad, N. Abd El-Salam, M. Cho, Solid-state symmetrical supercapacitor based on hierarchical flower-like nickel sulfide with shape-controlled morphological evolution, *Electrochim. Acta* 268 (2018) 82-93.
- [35] M. Yu, X. Li, Y. Ma, R. Liu, J. Liu, S. Li, Nanohoneycomb-like manganese cobalt sulfide/three dimensional graphene-nickel foam hybrid electrodes for high-rate capability supercapacitors, *Appl. Surf. Sci.* 396 (2017) 1816-1824.
- [36] J. Yang, Y. Zhang, C. Sun, G. Guo, W. Sun, W. Huang, Q. Yan, X. Dong, Controlled synthesis of zinc cobalt sulfide nanostructures in oil phase and their potential applications in electrochemical energy storage, *J. Mater. Chem. A* 3 (2015) 11462-11470.
- [37] B. Zhang, G. Yang, C. Li, K. Huang, J. Wu, S. Hao, J. Feng, D. Peng, Y. Huang, Phase controllable fabrication of zinc cobalt sulfide hollow polyhedra as high-performance electrocatalysts for the hydrogen evolution reaction, *Nanoscale* 10 (2018) 1774-1778.
- [38] C. Cheng, D. Kong, C. Wei, W. Du, J. Zhao, Y. Feng, Q. Duan, Self-template synthesis of hollow ellipsoid Ni-Mn sulfides for supercapacitors, electrocatalytic oxidation of glucose and water treatment, *Dalton Trans.* 46 (2017) 5406-5413.

- [39] T. Zhu, L. Zhu, J. Wang, G. Ho, In situ chemical etching of tunable 3D Ni<sub>3</sub>S<sub>2</sub> superstructures for bifunctional electrocatalysts for overall water splitting, *J. Mater. Chem. A* 4 (2016) 13916-13922.
- [40] M. Li, J. Cheng, F. Liu, X. Zhang, In situ growth of nickel-cobalt oxyhydroxide/oxide on carbon nanotubes for high performance supercapacitors, *Electrochim. Acta* 178 (2015) 439-446.
- [41] L. Hou, Y. Shi, S. Zhu, M. Rehan, G. Pang, X. Zhang, C. Yuan, Hollow mesoporous hetero-NiCo<sub>2</sub>S<sub>4</sub>/Co<sub>9</sub>S<sub>8</sub> submicro-spindles: unusual formation and excellent pseudocapacitance towards hybrid supercapacitors, *J. Mater. Chem. A* 3 (2017) 133-144.
- [42] X. Xiong, B. Zhao, D. Ding, D. Chen, C. Yang, Y. Lei, M. Liu, One-step synthesis of architectural Ni<sub>3</sub>S<sub>2</sub> nanosheet-on-nanorods array for use as high-performance electrodes for supercapacitors, *NPG Asia Mater.* 8 (2016) 1-7.
- [43] F. Chen, H. Wang, S. Ji, V. Linkov, R. Wang, High-performance all-solid-state asymmetric supercapacitors based on sponge-like NiS/Ni<sub>3</sub>S<sub>2</sub> hybrid nanosheets, *Mater. Today Energy* 11 (2019) 211-217.
- [44] J. Wang, K. Y. Ma, J. Zhang, F. Liu, J. P. Cheng, Template-free synthesis of hierarchical hollow NiS<sub>x</sub> microspheres for supercapacitor, *J. Colloid Interf. Sci.* 507 (2017) 290-299.
- [45] G. Park, J. Cho, Y. Kang, Sodium-ion storage properties of nickel sulfide hollow nanospheres/reduced graphene oxide composite powders prepared by a spray drying process and the nanoscale Kirkendall effect, *Nanoscale* 7 (2015) 16781-16788.
- [46] Y. Lv, A. Liu, Z. Shi, H. Che, J. Mu, Z. Guo, X. Zhang, Construction of hierarchical zinc cobalt sulfide@nickel sulfide core-shell nanosheet arrays for high-performance asymmetric solid-state supercapacitors, *Chem. Eng. J.* 349 (2018) 397-407.

- [47] C. Cheng, X. Zhang, C. Wei, Y. Liu, C. Cui, Q. Zhang, D. Zhang, Mesoporous hollow ZnCo<sub>2</sub>S<sub>4</sub> core-shell nanospheres for high performance supercapacitors, *Ceram. Int.* 44 (2018) 17464-17472.
- [48] X. Li, J. Bai, B. Zhou, X. Yuan, X. Zhang, L. Liu, High Performance of 3D Symmetric Flowerlike Sb<sub>2</sub>S<sub>3</sub> Nanostructures in Dye-Sensitized Solar Cells, *Chem.* 24 (2018) 11444-11450.
- [49] J. Yan, J. Liu, Z. Fan, T. Wei, L. Zhang, High-performance supercapacitor electrodes based on highly corrugated graphene sheets, *Carbon* 50 (2012) 2179-2188.
- [50] Q. Wang, J. Yan, Y. Xiao, T. Wei, Z. Fan, M. Zhang, X. Jing, Interconnected porous and nitrogen-doped carbon network for supercapacitors with high rate capability and energy density, *Electrochim. Acta* 114 (2013) 165-172.
- [51] X. Tian, C. Cheng, L. Qian, B. Zheng, H. Yuan, S. Xie, D. Xiao, M. Choi, Microwave-assisted non-aqueous homogenous precipitation of nanoball-like mesoporous  $\alpha$ -Ni(OH)<sub>2</sub> as a precursor for NiO<sub>x</sub> and its application as a pseudocapacitor, *J. Mater. Chem.* 22 (2012) 8029-8035.
- [52] X. Wang, J. Hao, Y. Su, F. Liu, J. An, J. Lian, A Ni<sub>1-x</sub>Zn<sub>x</sub>S/Ni foam composite electrode with multi-layers: one-step synthesis and high supercapacitor performance, *J. Mater. Chem. A* 4 (2016) 12929-12939.
- [53] J. Wang, S. Wang, Z. Huang, Y. Yu, High-performance NiCo<sub>2</sub>O<sub>4</sub>@Ni<sub>3</sub>S<sub>2</sub> core/shell mesoporous nanothorn arrays on Ni foam for supercapacitors, *J. Mater. Chem. A* 2 (2014) 17595-17601.

- [54] J. He, Y. Chen, P. Li, F. Fu, Z. Wang, W. Zhang, Self-assembled CoS<sub>2</sub> nanoparticles wrapped by CoS<sub>2</sub>-quantum-dots-anchored graphene nanosheets as superior-capability anode for lithium-ion batteries, *Electrochim. Acta* 182 (2015) 424-429.
- [55] A. Ivanishchev, I. Bobrikov, I. Ivanishcheva, O. Ivanshina, Study of structural and electrochemical characteristics of LiNi<sub>0.33</sub>Mn<sub>0.33</sub>Co<sub>0.33</sub>O<sub>2</sub> electrode at lithium content variation, *J. Electroanal. Chem.* 821 (2018) 140-151.
- [56] A. Ivanishchev, A. Churikov, I. Ivanishcheva, A. Ushakov, M. Sneha, P. Babbar, A. Dixit, Models of lithium transport as applied to determination of diffusion characteristics of intercalation electrodes, *Russ. J. Electrochem.* 53 (2017) 706-712.
- [57] K. Tao, X. Han, Q. Cheng, Y. Yang, Z. Yang, Q. Ma, L. Han, Zinc cobalt sulfide nanosheets array derived from 2D bimetallic metal-organic frameworks for high-performance supercapacitor, *Chem.-EUR. J.* 24 (2018) 12584-12591.
- [58] S. Min, C. Zhao, G. Chen, X. Qian, One-pot hydrothermal synthesis of reduced graphene oxide/Ni(OH)<sub>2</sub> films on nickel foam for high performance supercapacitors, *Electrochim. Acta* 115 (2014) 155-164.
- [59] Y. Zhu, Z. Wu, M. Jing, X. Yang, W. Song, X. Ji, Mesoporous NiCo<sub>2</sub>S<sub>4</sub> nanoparticles as high-performance electrode materials for supercapacitors, *J. Power Sources* 273 (2015) 584-590.
- [60] F. Luo, J. Li, H. Yuan, D. Xiao, Rapid synthesis of three-dimensional flower-like cobalt sulfide architectures by microwave assisted heating method for high-performance supercapacitors, *Electrochim. Acta* 123 (2014) 183-189.

- [61] A. Namdarian, A. Tabrizi, A. Maselena, A. Mohammadi, S. Moosavifard, One step synthesis of rGO-Ni<sub>3</sub>S<sub>2</sub> nano-cubes composite for high-performance supercapacitor electrodes, *Int. J. Hydrogen Energ.* 43 (2018) 17780-17787.
- [62] C. S. Dai, P. Y. Chien, J. Y. Lin, S. W. Chou, W. K. Wu, P. H. Li, K. Y. Wu, T. W. Lin, Hierarchically structured Ni<sub>3</sub>S<sub>2</sub>/carbon nanotube composites as high performance cathode materials for asymmetric supercapacitors, *ACS Appl. Mater. Inter.* 5 (2013) 12168-12174.
- [63] G. Li, M. Liu, M. Wu, P. Liu, Z. Zhou, S. Zhu, R. Liu, L. Han, MOF-derived self-sacrificing route to hollow NiS<sub>2</sub>/ ZnS nanospheres for high performance supercapacitors, *RSC* 6 (2016) 103517–103522.
- [64] Z. Dai, X. Zang, J. Yang, C. Sun, W. Si, W. Huang, X. Dong, Template Synthesis of Shape-Tailorable NiS<sub>2</sub> Hollow Prisms as High-Performance Supercapacitor Materials, *ACS Appl. Mater. Inter.* 7 (2015) 25396-25401.
- [65] X. Mao, W. Wang, Z. Wang, Hydrothermal Synthesis of Zn<sub>x</sub>Ni<sub>1-x</sub>S nanosheets for Hybrid Supercapacitor Applications, *ChemPlusChem* 82 (2017) 1145-1152.
- [66] T. Brousse, D. Bélanger, J. Longd, To Be or Not To Be Pseudocapacitive?, *J. Electrochem. Soc.* 162 (2015) A5185-A5189.
- [67] J. Shi, X. Li, G. He, L. Zhang, M. Li, Electrodeposition of high-capacitance 3D CoS/graphene nanosheets on nickel foam for high-performance aqueous asymmetric supercapacitors, *J. Mater. Chem. A* 3 (2015) 20619-20626.
- [68] Y. Zhang, N. Cao, S. Szunerits, A. Addad, P. Roussel, R. Boukherroub, Fabrication of ZnCoS nanomaterial for high energy flexible asymmetric supercapacitors, *Chem. Eng. J.* 374 (2019) 347-358.